

Article

A Framework for Determining the Optimal Vibratory Frequency of Graded Gravel Fillers Using Hammering Modal Approach and ANN

Xianpu Xiao ^{1,2}, Taifeng Li ^{1,*}, Feng Lin ¹, Xinzhi Li ², Zherui Hao ³ and Jiashen Li ³

¹ China Academy of Railway Sciences Co., Ltd., Beijing 100081, China; xiao18388517746@163.com (X.X.); linfeng_tieke@163.com (F.L.)

² Department of Civil Engineering, Shijiazhuang Tiedao University, Shijiazhuang 050043, China; lixinzhistdu@163.com

³ Department of Civil Engineering, Central South University, Changsha 410075, China; zheruihao@csu.edu.cn (Z.H.); 224812312@csu.edu.cn (J.L.)

* Correspondence: taifeng_tieke@163.com; Tel.: +86-183-8851-7746

Abstract: To address the uncertainty of optimal vibratory frequency f_{ov} of high-speed railway graded gravel (HRGG) and achieve high-precision prediction of the f_{ov} , the following research was conducted. Firstly, commencing with vibratory compaction experiments and the hammering modal analysis method, the resonance frequency f_0 of HRGG fillers, varying in compactness K , was initially determined. The correlation between f_0 and f_{ov} was revealed through vibratory compaction experiments conducted at different vibratory frequencies. This correlation was established based on the compaction physical–mechanical properties of HRGG fillers, encompassing maximum dry density ρ_{dmax} , stiffness K_{rd} , and bearing capacity coefficient K_{20} . Secondly, the gray relational analysis algorithm was used to determine the key feature influencing the f_{ov} based on the quantified relationship between the filler feature and f_{ov} . Finally, the key features influencing the f_{ov} were used as input parameters to establish the artificial neural network prediction model (ANN-PM) for f_{ov} . The predictive performance of ANN-PM was evaluated from the ablation study, prediction accuracy, and prediction error. The results showed that the ρ_{dmax} , K_{rd} , and K_{20} all obtained optimal states when f_{ov} was set as f_0 for different gradation HRGG fillers. Furthermore, it was found that the key features influencing the f_{ov} were determined to be the maximum particle diameter d_{max} , gradation parameters b and m , flat and elongated particles in coarse aggregate Q_e , and the Los Angeles abrasion of coarse aggregate LAA. Among them, the influence of d_{max} on the ANN-PM predictive performance was the most significant. On the training and testing sets, the goodness-of-fit R^2 of ANN-PM all exceeded 0.95, and the prediction errors were small, which indicated that the accuracy of ANN-PM predictions was relatively high. In addition, it was clear that the ANN-PM exhibited excellent robust performance. The research results provide a novel method for determining the f_{ov} of subgrade fillers and provide theoretical guidance for the intelligent construction of high-speed railway subgrades.



Citation: Xiao, X.; Li, T.; Lin, F.; Li, X.; Hao, Z.; Li, J. A Framework for Determining the Optimal Vibratory Frequency of Graded Gravel Fillers Using Hammering Modal Approach and ANN. *Sensors* **2024**, *24*, 689. <https://doi.org/10.3390/s24020689>

Academic Editor: Mohammad Noori

Received: 16 November 2023

Revised: 10 January 2024

Accepted: 19 January 2024

Published: 22 January 2024

Keywords: high-speed railway subgrade; vibration compaction; optimal vibration frequency; key features; ANN



Copyright: © 2024 by the authors. Licensee MDPI, Basel, Switzerland. This article is an open access article distributed under the terms and conditions of the Creative Commons Attribution (CC BY) license (<https://creativecommons.org/licenses/by/4.0/>).

1. Introduction

The compaction quality control of high-speed railway graded gravel (HRGG) was a crucial factor influencing the service performance of the subgrade [1–3]. Vibratory compaction was the mainstream method in subgrade construction, where the vibration frequency was closely related to compaction quality control. Unreasonable vibration frequencies could lead to poor control of subgrade compaction quality, which caused various types of subgrade diseases, such as uneven settlement [4,5] and permanent deformation [6,7]. Meanwhile, there has been limited research on the intelligent prediction of the optimal

vibratory frequency f_{ov} for vibratory compaction, which has hindered the development of intelligent subgrade construction [8]. Hence, proposing a method for determining the subgrade compaction f_{ov} and achieving intelligent prediction of the compaction f_{ov} are of great guiding significance for improving the service performance of the subgrade and developing intelligent construction for high-speed railway subgrades.

Existing research highlights a robust correlation between vibration frequency and the dry density ρ_d of coarse-grained soil fillers. Through plate vibration compaction experiments, Wang et al. [9] and Ji et al. [10] identified an optimal vibration frequency range (25~27 Hz) under varying excitation forces, resulting in the attainment of maximum dry density during the compaction of coarse-grained soil fillers. Moreover, in vibration compaction experiments, Xie et al. [11] observed that employing the optimal frequency reduces HRGG filler crushing, contributing to its optimal mechanical performance. Furthermore, based on indoor experiments, Ye et al. [12] found that when the vibration frequency (25~30 Hz) approaches the resonance frequency of the fillers, the structure of coarse-grained soil fillers becomes more compact, resulting in the maximum dry density. It was observed that there existed an optimal vibration frequency f_{ov} within coarse-grained fillers during vibratory compaction, which resulted in the optimal compaction state of the fillers. Additionally, the study indicates a close relationship between the resonance frequency f_0 of the fillers and the optimal vibration frequency [13,14]. Furthermore, to improve the efficiency of vibratory compaction for coarse-grained fillers, many scholars conducted research on determining the f_{ov} for coarse-grained fillers. Xie et al. [15] concluded that the f_0 of coarse-grained soil fillers increased with compaction density. Additionally, it was observed that the compaction performance of the fillers was optimal when the vibration frequency matched the f_0 . Hence, it was urgent to investigate the relationship between f_0 and compacted f_{ov} , and propose a new method to determine the f_{ov} .

With the development of intelligent compaction technology, the high-precision prediction of vibratory compaction parameters became a crucial part of intelligent subgrade construction [16,17]. Recently, many scholars have established the relationship between compaction parameters and filler features using linear regression models [18]. Nevertheless, there was a clear non-linear relationship between f_{ov} and filler characteristics, and the accuracy of this model was still open to question. In previous studies, machine learning (ML), recognized for its non-linear mapping capability, has proven to be an effective approach for predicting parameters in vibratory compaction. For example, Isik [19] applied the artificial neural network (ANN) algorithm to forecast compaction parameters in fine-grained soil and substantiated the suitability of the ANN algorithm by utilizing accuracy and error metrics such as goodness-of-fit (R^2) and mean square error (MSE). Zaman et al. [20] established an ANN model to quantify the relationship between the elastic modulus and stress state of roadbed-graded aggregates. Additionally, Xie et al. [21] found that the ANN model had a better predictive capability for the optimal moisture content of HRGG fillers during vibratory compaction. All the above studies employed the ANN model to predict vibratory compaction parameters, and the prediction results were favorable, which indicated that the ANN model exhibited a strong predictive capability for vibratory compaction parameters. Additionally, considering the multitude of factors influencing f_{ov} , taking the key feature influencing the f_{ov} as input features for the prediction model could reduce the sample space dimension, enhance the predictive performance of the model, and further improve prediction accuracy [22,23]. Nevertheless, there was a lack of systematic characterization of the performance of coarse-grained fillers, especially the relationship between gradation, particle shape, particle crushing, and f_{ov} . Hence, it was necessary to determine the key feature influencing the f_{ov} .

In summary, to address the issue of uncertainty in the vibration compaction f_{ov} of HRGG fillers and achieve intelligent prediction of f_{ov} , this paper conducts the following research. Firstly, based on vibratory compaction experiments and the hammering modal analysis method, the f_0 of different compaction degrees K of fillers was determined. Furthermore, the correlation between f_0 and f_{ov} was revealed based on compaction experiments

at different vibratory frequencies and based on the maximum dry density $\rho_{d_{\max}}$, dynamic stiffness K_{rd} , and bearing capacity coefficient K_{20} of the fillers. Secondly, the gray relational analysis algorithm was used to determine the key feature influencing the f_{ov} based on the quantified relationship between the filler feature and f_{ov} . Finally, the key features influencing the f_{ov} were used as input parameters to establish the artificial neural network prediction model (ANN-PM) for f_{ov} , and the predictive performance of ANN-PM was evaluated from the prediction accuracy and error. This research not only determined the f_{ov} of HRGG fillers through the hammering modal analysis method, but also achieved intelligent prediction of f_{ov} based on the ANN model. This provides a theoretical foundation for intelligent construction in high-speed railway subgrades.

2. The Method of Determining f_{ov}

2.1. Material

As shown in Figure 1a, the HRGG fillers used in this experiment were surface subgrade fillers of the high-speed railway, which consisted of crushed limestone gravel. Based on the Code for Railway Subgrade Design (TB 10001-2016) [24], the gradation of fillers should meet the following requirements: the maximum particle diameter $d_{\max} \leq 60$ mm, the coefficient of uniformity $C_u \geq 15$, and the coefficient of curvature $C_c = 1\sim 3$. Hence, as shown in Figure 1b, three types of gradation were selected as experimental fillers: skeleton pore gradation G1 ($d_{\max} = 45$ mm, $C_u = 18.2$, $C_c = 1.374$), skeleton dense gradation G2 ($d_{\max} = 45$ mm, $C_u = 40.0$, $C_c = 2.243$), and suspended dense gradation G3 ($d_{\max} = 40.5$ mm, $C_u = 53.333$, $C_c = 1.2$).

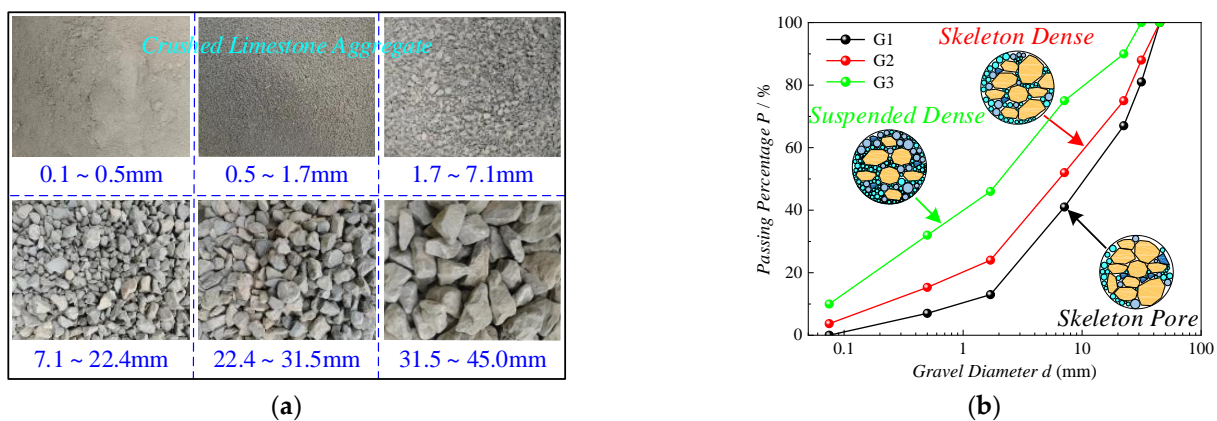


Figure 1. Experimental material: (a) crushed limestone aggregate, (b) three typical gradation curves.

2.2. Experimental Design

Vibratory compaction experiments were conducted using an improved large-scale intelligent vibratory compactor [15]. The equipment was not only equipped with four adjustable parameters, containing the vibratory frequency f (0~80 Hz), static load m_p (0~400 kg), eccentricity distance r_e (0~8 cm), and eccentric mass m_e (0~2.4 kg), but also its compaction mechanism was similar to the on-site roller compaction. As shown in Figure 2a, it was important to note that compared with the conventional vibratory compactor, this equipment embedded displacement sensors, hall sensors, and vibratory acceleration sensors. Furthermore, based on Equations (1) and (2), the real-time output of the dry density ρ_d curve and dynamic stiffness K_{rd} curve can be obtained.

$$\rho_d = \frac{mg}{\pi D_c^2 (h_0 - S_n)} \quad (1)$$

$$K_{rd} = \frac{m_e r_e \omega^2 \sin(\Delta\varphi) + m_p g - m_d \ddot{x}|_{\dot{x}=0}}{x|_{\dot{x}=0}} \quad (2)$$

where m is the mass of fillers; D_c is the internal diameter of the compaction cylinder; h_0 is the pavement thickness; S_n is the displacement rate of fillers; m_e is the mass of the eccentric block; r_e is the eccentricity; ω is the rotation speed of the eccentric block; $\Delta\varphi$ is the lag phase angle, which is obtained from the hall sensor; m_p is the mass of the weight block; m_d is the mass of the vibratory system; x is the displacement of the vibratory system, which is obtained from the displacement sensors; \ddot{x} is the acceleration of the vibratory system, which is obtained from the acceleration sensors.

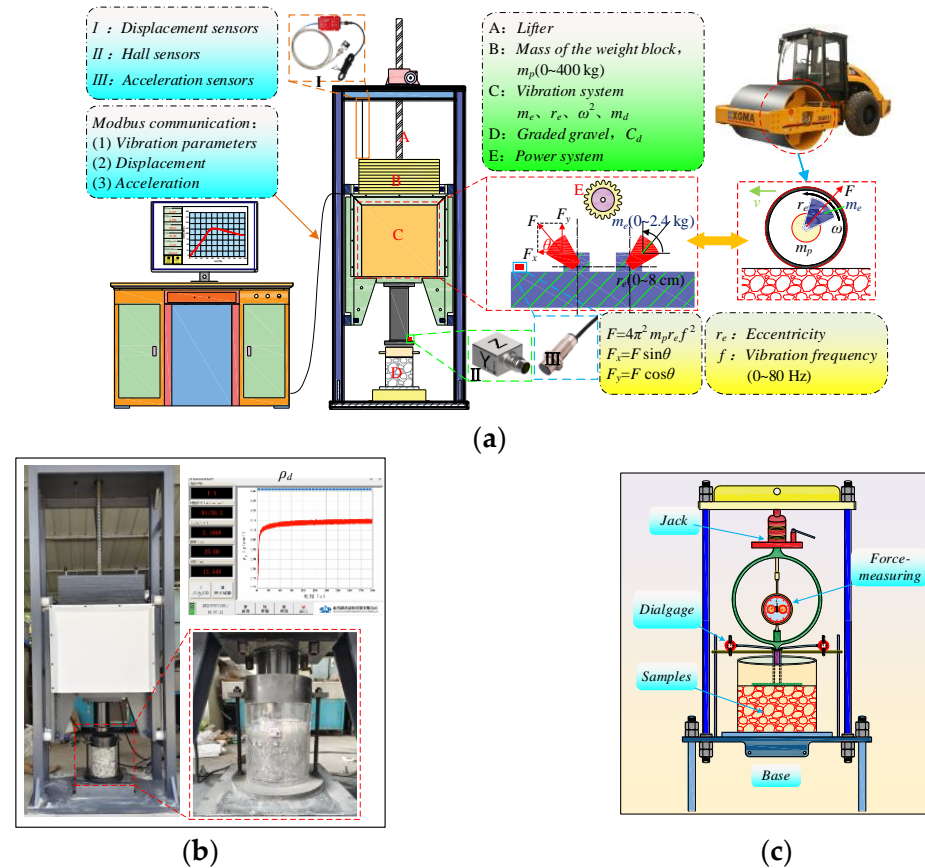


Figure 2. Experimental equipment: (a) intelligent compaction equipment, (b) experimental data collection, and (c) indoor flatbed loading equipment.

Applying the method proposed by Xie et al. [25] to determine the maximum dry density $\rho_{d_{\max}}$, the compaction degree K of HRGG fillers can be calculated in real time by Equation (3). Hence, as shown in Figure 2b, the fillers with different K can be accurately obtained by controlling the vibratory compaction time. Additionally, as shown in Figure 2c, to validate the efficacy of the K_{rd} obtained from the intelligent vibratory compactor, the bearing capacity coefficient K_{30} was used to evaluate the mechanical properties of the fillers. To ensure consistency between the indoor K_{30} and field experiments, it is necessary to scale down the K_{30} of the field using the theory of similarity. The K_{30} in this experiment was computed by Equation (4), which was derived based on the similarity coefficient for K_{30} proposed by Xie et al. [11].

$$K = \frac{\rho_d}{\rho_{d_{\max}}} \quad (3)$$

$$K_{30} = K_{20} = \frac{\sigma_{0.84}}{S_{0.84}} \quad (4)$$

where $S_{0.84}$ is a sinkage of 0.84 mm and $\sigma_{0.84}$ is the load strength corresponding to a sinkage of 0.84 mm.

To improve the compaction quality and control the particle crushing, the parameters for the vibratory compaction experiments were selected using the optimal parameter determination method based on the resonance frequency f_0 proposed by Xie et al. [25]. The vibratory frequency f was set to the f_0 of the fillers, the excitation force $F_0/m_p < 1.9$, the moisture content ω was set to the critical moisture content of the fillers, the diameter-to-diameter ratio (D_c/d_{\max}) was set to 3.9, and the thickness-to-diameter ratio (h_0/d_{\max}) was set to 3.5. Hence, in this paper, the parameters for the vibratory compaction experiments were shown in Table 1.

Table 1. The parameters of vibratory compaction experiments.

Gradation	f (Hz)	ω (%)	m_p (kg)	r_e (mm)	m_e (kg)	D_c (mm)	h_0 (mm)
G1	40	3.6	600	18.0	4.7	200	155
G2	34	4.0	600	25.1	4.7	200	155
G3	26	5.4	600	44.4	4.7	200	155

As shown in Figure 3, the vibratory compaction experiments were primarily divided into three steps. (1) Sample preparation: the initial fillers were classified based on particle size through sieving tests, and the samples were prepared according to the experimental gradation. (2) Vibratory compaction: experiments were conducted using the intelligent vibratory compactor, and the ρ_d and K_{rd} of the HRGG fillers were collected in real time. (3) K_{20} testing: the K_{20} of the HRGG fillers after vibratory compaction was tested based on a plate load test.

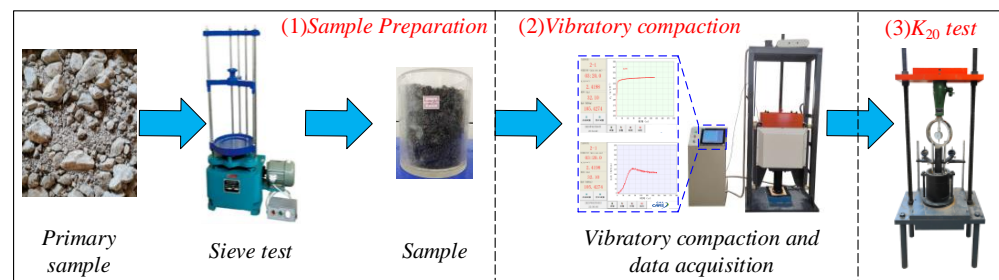


Figure 3. The diagram of vibratory compaction experiments.

2.3. The Tests of Determining f_0

The post-compaction f_0 of the HRGG fillers was obtained from the hammering modal analysis method [26]. As shown in Figure 4, the hammering modal experiments were primarily divided into three steps. (1) Demold: the complete compacted HRGG fillers were obtained using demolding equipment after the plate load test. (2) Installation of acceleration sensors: a triaxial accelerometer was installed at the top of the fillers and connected to the DH5922D dynamic signal acquisition equipment. (3) Collection of hammer impact acceleration signals: a rubber hammer was used to strike the top of the fillers, and the acceleration signals of the fillers during the strike were recorded in real time. To ensure the reliability of the signals, the hammering modal experiments for fillers with different K were repeated three times. Based on the acceleration signals of the fillers, the f_0 with different K of fillers was determined by the hammering modal analysis method.

Figure 5 shows the hammering modal method analysis process based on G2 type HRGG fillers. Figure 5a shows the time-domain amplitude of the acceleration signal. The acceleration amplitude gradually weakened after reaching the peak until stabilized, indicating the fillers' vibratory feature during the strike. The initial peak indicated a rapid response of the fillers to the hammering, while the weakening process indicated that the hammering energy gradually dissipated within the fillers until stabilized. As shown in Figure 5b, the time-domain acceleration signal was subjected to Fourier transformation to obtain the acceleration signal spectrum. It was observed that the acceleration reached the

peak at a frequency of 33 Hz, which indicated a significant vibratory response of the fillers at this frequency. Hence, 33 Hz was determined as the first f_0 of the G2 type HRGG fillers.

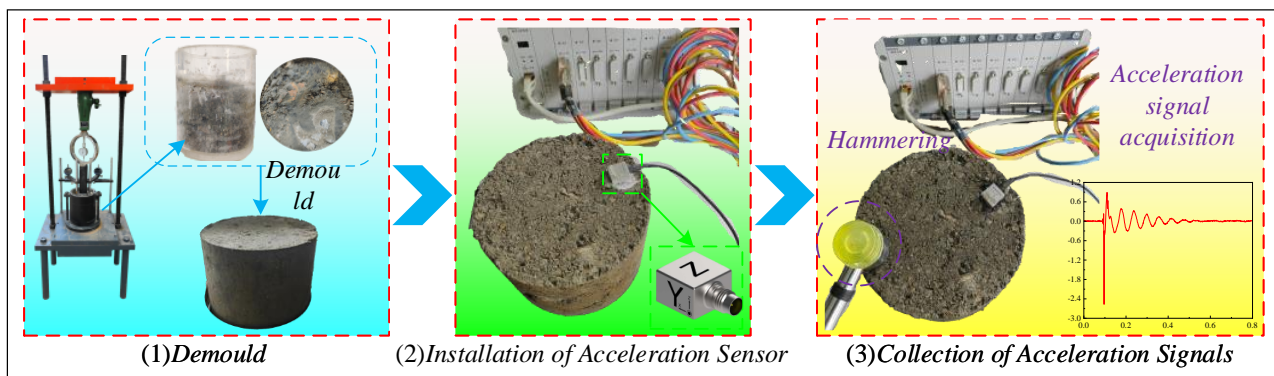


Figure 4. The diagram of hammer impact experiments.

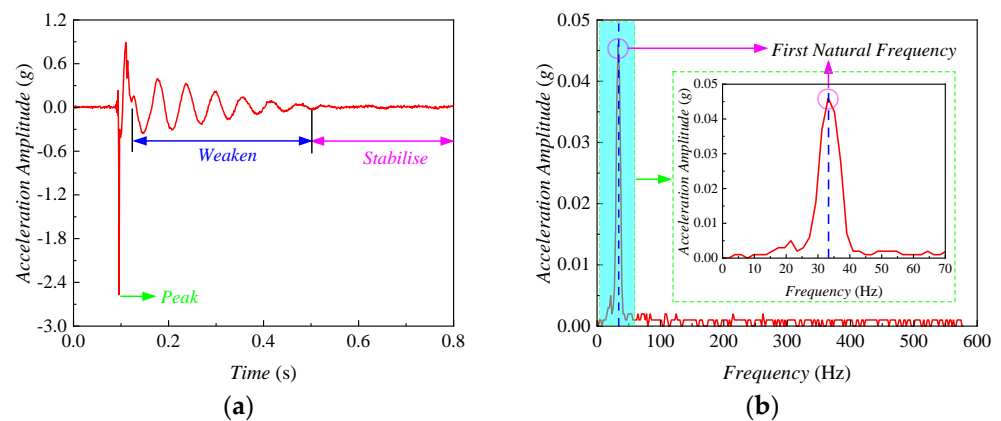


Figure 5. Hammer impact modal analysis: (a) acceleration time-domain amplitude, (b) acceleration amplitude-frequency spectrum.

As shown in Figure 6, hammering modal experiments were conducted on HRGG fillers with different K and gradation, revealing the relationship between gradation, K , and f_0 . As shown in Figure 6a, with the K increasing, the f_0 of all three fillers showed a pattern of “rapid increase—slower increase”, and when $K > 0.95$, f_0 tended to stabilize. As shown in Figure 6b, when $K = 0.96$, the filler gradation transitioned from G1 to G3, and the coarse particle content gradually decreased, which led to a gradual reduction in f_0 .

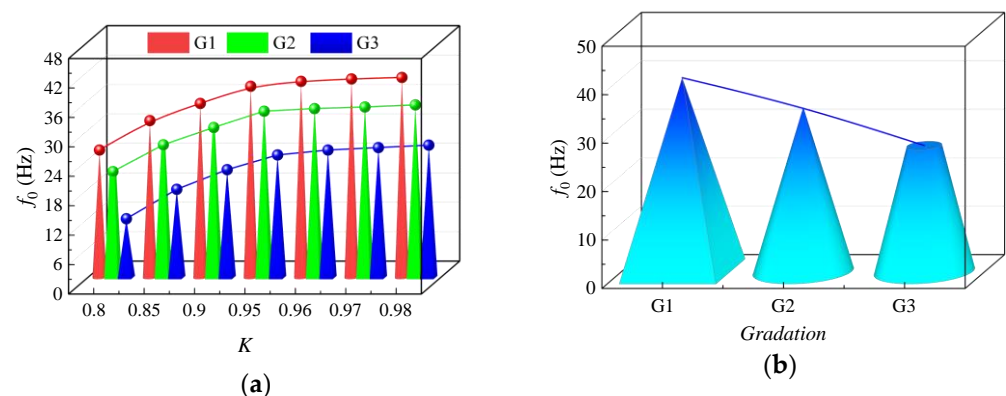


Figure 6. Relationship between K , gradation, and f_0 : (a) relationship between K and f_0 , (b) relationship between gradation and f_0 when $K = 0.96$.

2.4. Relationship between f_0 and f_{ov}

In summary, the f_0 of HRGG fillers with different K had been determined by hammering modal experiments. Vibratory compaction experiments were conducted with vibratory frequencies set at 20, 25, 30, 35, 40, and 45 Hz. Furthermore, the relationship between f_0 and f_{ov} was explored by the parameters K_{rd} , K_{20} , and ρ_d of the fillers.

As shown in Figure 7, the evolution patterns of K_{rd} , K_{20} , and ρ_d for the HRGG fillers under different vibratory frequencies during the vibratory compaction were obtained. As shown in Figure 7a, the K_{rd} of fillers at different vibratory frequencies all exhibited a pattern of “rapid increase—slower decrease”, indicating the presence of an “inflection point” in the K_{rd} curve. As shown in Figure 7b, when the vibratory frequency was set as f_0 , the K_{20} also reached the maximum value at the “inflection point” of K_{rd} . As shown in Figure 7c, the ρ_d of fillers at different vibratory frequencies all showed a pattern of “rapid increase—slower increase”. Nevertheless, it was difficult to determine the maximum dry density ρ_{dmax} based on the evolution pattern of ρ_d . Hence, ρ_{dmax} could be determined on the ρ_d curve by the vibratory time T_{ip} corresponding to the “inflection point” on the K_{rd} curve [25].

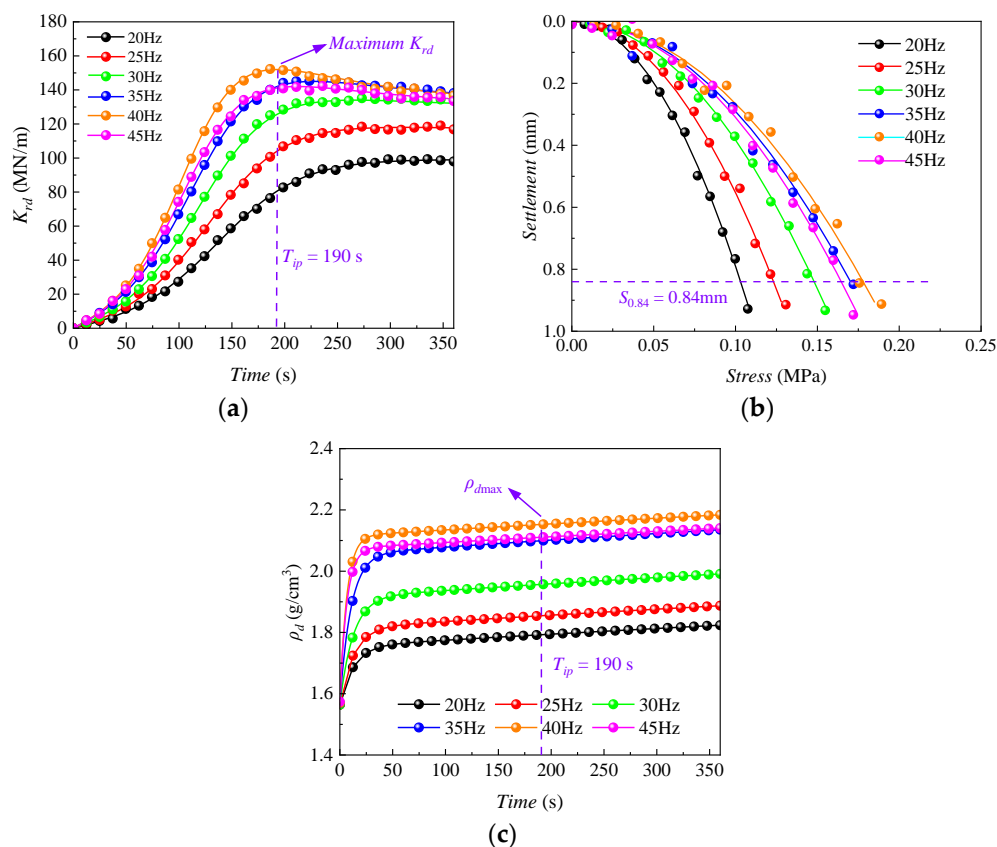


Figure 7. Evolution of K_{rd} , K_{20} , and ρ_d of graded gravel (G1) under different vibratory frequencies: (a) K_{rd} time history curve, (b) K_{20} time history curve, (c) ρ_d time history curve.

As shown in Figure 8, the relationships between K_{rd} , K_{20} , and ρ_{dmax} of HRGG fillers, in relation to vibratory frequency and gradation, were obtained from vibratory compaction experiments. As shown in Figure 8a, when the vibratory frequency was f_0 , fillers with different gradations all exhibited the maximum K_{rd} . Similarly, as shown in Figure 8b,c, when the vibratory frequency was f_0 , the K_{20} and ρ_{dmax} all reached maximum values, which was consistent with the evolution patterns of K_{rd} . The above experimental results indicated that the mechanical and physical properties of the compacted fillers were optimal when the vibratory frequency was f_0 , further indicating that f_0 was the optimal compaction frequency.

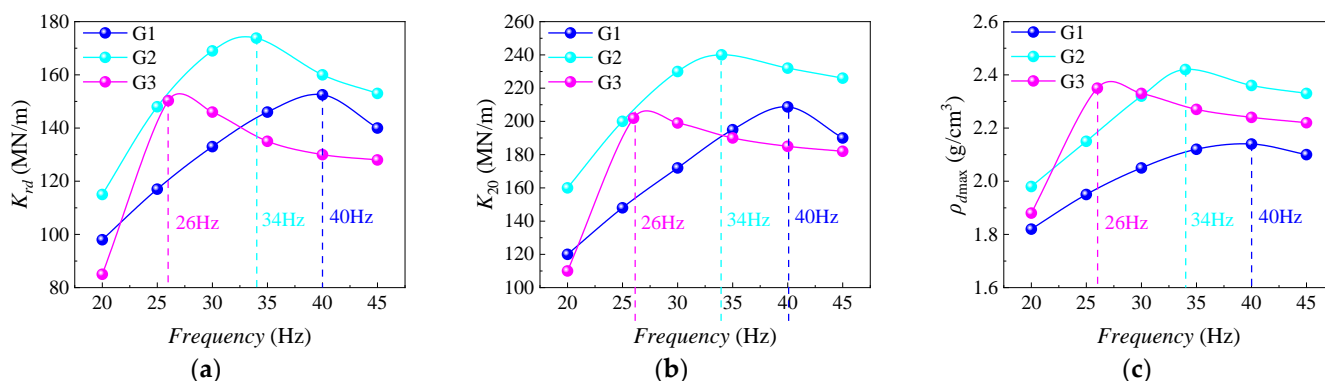


Figure 8. Relationship between vibratory frequency and maximum K_{rd} , K_{20} , and ρ_{dmax} : (a) relationship between vibratory frequency and maximum K_{rd} , (b) relationship between vibratory frequency and K_{20} , and (c) relationship between vibratory frequency and ρ_{dmax} .

3. ANN-Based Predictive Model for f_{ov}

3.1. Key Feature of f_{ov}

According to the Chinese Code for Design of Railway Earth Structure (TB 10001–2016) [1], the performance feature of the fillers include gradation, particle shape, and particle crushing, such as C_u , C_c , d_{max} , three typical particle diameters ($d \leq 0.5$ mm, $d = 0.5 \sim 1.7$ mm, $d \geq 1.7$ mm), the Los Angeles abrasion of coarse aggregate LAA , flat and elongated particles in coarse aggregate Q_e , the water absorption of coarse aggregate W_{ac} , the water absorption of fine aggregate W_{fc} , the liquid limit of fine aggregate LL , and the plastic limit of fine aggregate PL . As shown in Figure 9, to identify the feature of influencing the f_{ov} , all features were tested in the vibratory compaction experiments based on the Railway Ballast (TB/T 2140-2008) [27] and Geotechnical Testing Procedures for Railway Engineering (TB 10102-2023) [28].

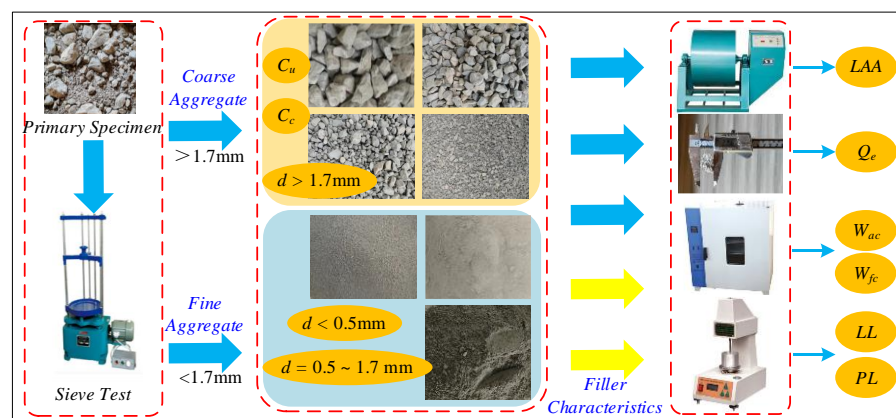


Figure 9. Performance feature experiments of fillers.

Recently, the relationship between all features and f_{ov} was still unclear. If all features influencing f_{ov} were inputted into the ML prediction model, this might have overshadowed the role of key features and increased the difficulty of model training. Hence, it was necessary to identify the key features influencing f_{ov} , and then input them into the ML prediction model to reduce the spatial dimension of the samples and enhance the efficiency of model training.

As shown in Figure 10a, Grey Relational Analysis (GRA) was a statistical method for analyzing multiple factors, which assessed the correlation of sequences based on the similarity of their curve shapes. The similarity in sequence curve shapes was positively correlated with sequence correlation [29]. Hence, the key feature of influencing the f_{ov}

could be determined based on GRA. As shown in Figure 10b and Table 2, the correlation coefficient R between each characteristic and f_{ov} was calculated. Generally, the feature could be considered as strongly correlated when $R > 0.6$. Thus, the feature strongly correlated with f_{ov} was as follows: d_{max} (0.75), $d < 0.5$ mm (0.73), $d \geq 1.7$ mm (0.71), $d = 0.5$ mm~1.7 mm (0.68), Q_e (0.66), LAA (0.64).

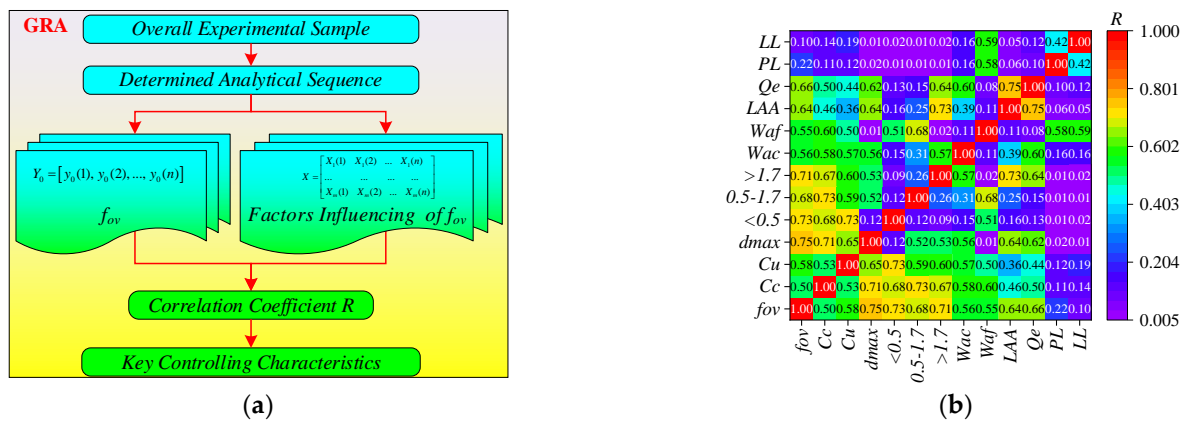


Figure 10. Based on the GRA algorithm analysis of f_{ov} key characteristics: (a) flowchart of GRA algorithm, (b) characterization analysis results.

Table 2. The correlation between different performance features of HRGG fillers and f_{ov} .

Performance feature	C_u	C_c	d_{max}	$d \leq 0.5$	$d = 0.5\sim 1.7$	$d \geq 1.7$	LAA	Q_e	W_{ac}	W_{af}	LL	PL
Correlation coefficient R	0.58	0.5	0.75	0.73	0.68	0.71	0.64	0.66	0.56	0.55	0.1	0.22

3.2. Dataset of ANN Model

The GRA algorithm explicitly determined the key feature influencing the f_{ov} . Nevertheless, it was difficult to provide a detailed description of the gradation feature for $d \geq 1.7$ mm, $d = 0.5$ mm~1.7 mm, and $d < 0.5$ mm, making it impractical for direct application in the ML prediction model. Hence, it was crucial to accurately quantify the gradation feature of the fillers. As shown in Equation (5), Wu et al. [30] proposed an equation that could describe the continuous gradation of coarse-grained soil. Thus, the three indicators of the gradation feature could be described by the two gradation characteristic parameters: b and m . Eventually, d_{max} , b , m , Q_e , and LAA were considered as the key features of influencing the f_{ov} and were used as input features for the ML prediction model.

$$P = \frac{1}{(1 - b) \left(\frac{d_{max}}{d}\right)^m + b} \times 100\% \tag{5}$$

where b and m are the gradation characteristic parameters.

To validate the reasonableness of Equation (5) in describing the gradation feature of HRGG fillers, as shown in Figure 11, the d_{max} was set to 60 mm, and different values were assigned to b and m , resulting in gradation curves of different forms. The slope of the gradation curve was primarily determined by m . When b was held constant, m was positively correlated with the slope of the gradation curve. Meanwhile, the shape of the gradation curve was mainly determined by b . When m was held constant, with the b increasing, the gradation curve gradually transitioned from “hyperbolic” to “reverse S-shaped”. In conclusion, the parameters m and b in the gradation equation, respectively determined the slope and shape of the gradation curve. The wide range of variation in the b and m allowed the gradation equation to reflect different forms of gradation curves. Hence, it was reasonable to use Equation (5) to describe the gradation feature of HRGG fillers.

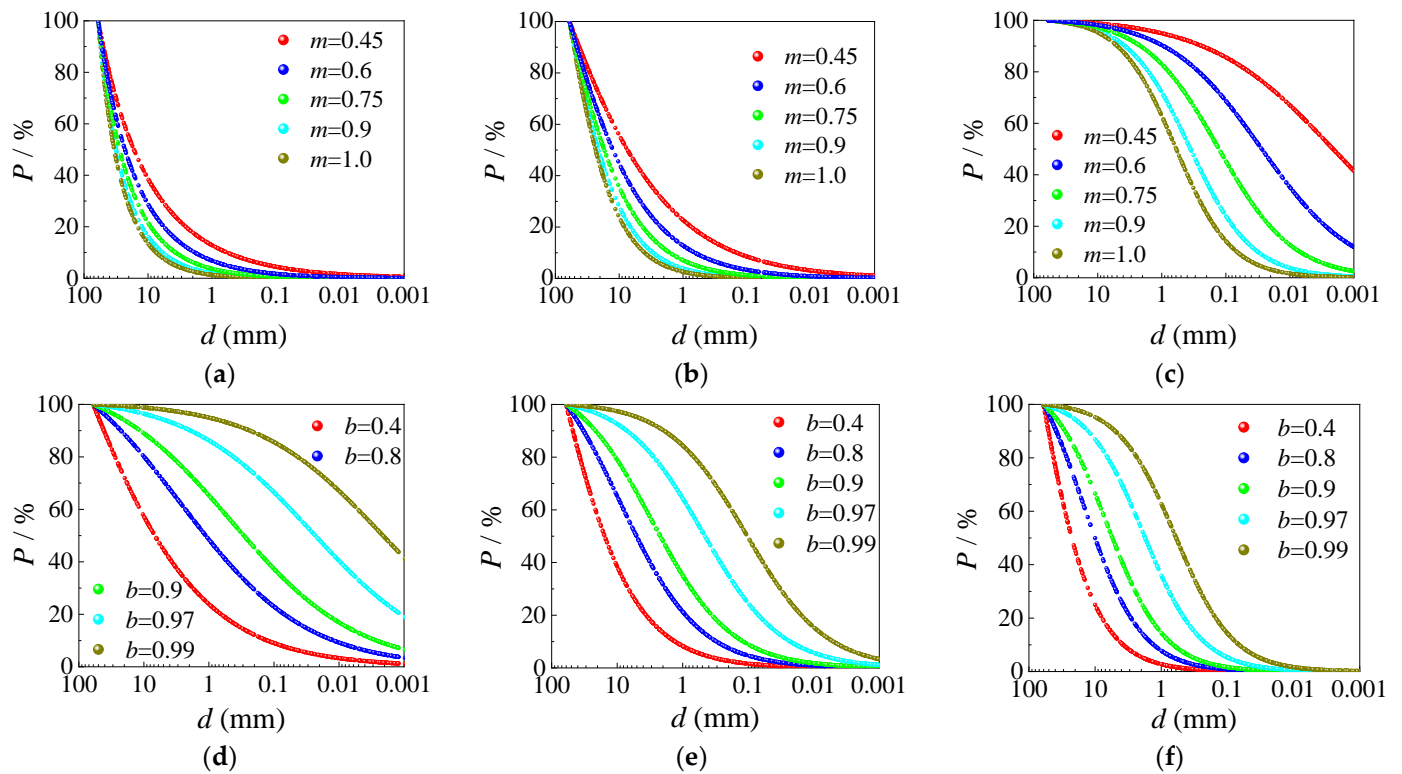


Figure 11. Relationship between gradation characteristic parameters and curve shape: (a) $b = -0.28$, (b) $b = 0.36$, (c) $b = 1.0$, (d) $m = 0.45$, (e) $m = 0.725$, and (f) $m = 1.0$.

The ML prediction model dataset was further constructed based on the five key features of influencing the f_{ov} . A dataset $D = \{(x_\rho, y_\rho)\}_{i=1}^N$ was established by analyzing the relationship between f_{ov} and the five key features for 333 sets of fillers with different gradations, where x_ρ represented the input feature consisting of the five key characteristics, and y_ρ represented the output feature consisting of f_{ov} . As shown in Figure 12, the relationships between the five key features and f_{ov} in the ML prediction model dataset were obtained by analysis.

3.3. Establishment and Evaluation of ANN-PM

As shown in Figure 13, Artificial Neural Network (ANN) was a typical ML algorithm [31–36] used for predictive analysis of the f_{ov} . Additionally, the ANN model was trained using the Adam optimizer algorithm [37,38]. During the training, the mean absolute error (MAE) was used as the objective function to calculate particle fitness, which could be calculated by Equation (6). As shown in Figure 14, the establishment of the ANN prediction model (ANN-PM) based on f_{ov} primarily involved three steps: (1) partitioning the dataset, (2) developing the ANN-PM based on the training set, (3) and evaluating the performance of the ANN-PM based on the testing set.

$$fitness = MAE = \frac{1}{n} \sum_{i=1}^n |y_i - \hat{y}_i| \quad (6)$$

where n is the sample size, y_i is the true value, and \hat{y}_i is the predicted value.

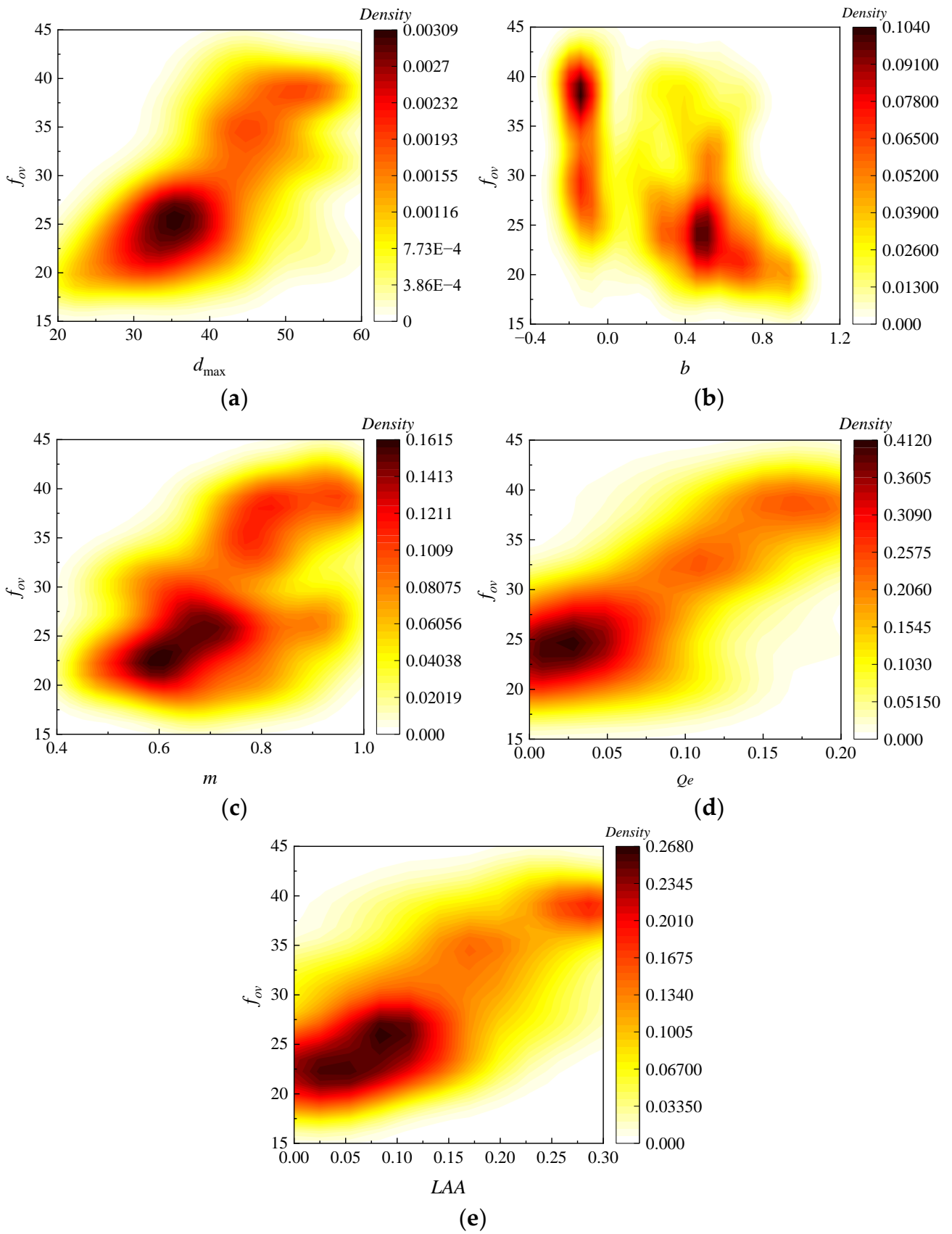


Figure 12. Relationship between the key features and f_{ov} : (a) d_{max} , (b) b , (c) m , (d) Q_e , and (e) LAA .

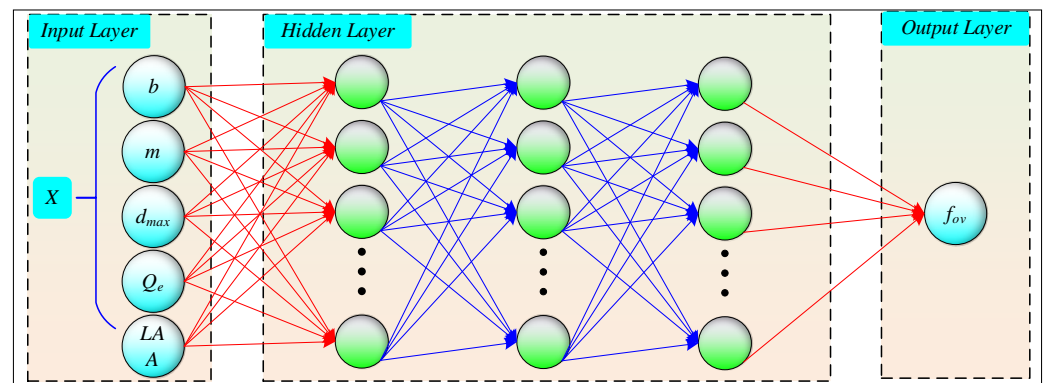


Figure 13. Architecture of artificial neural network.

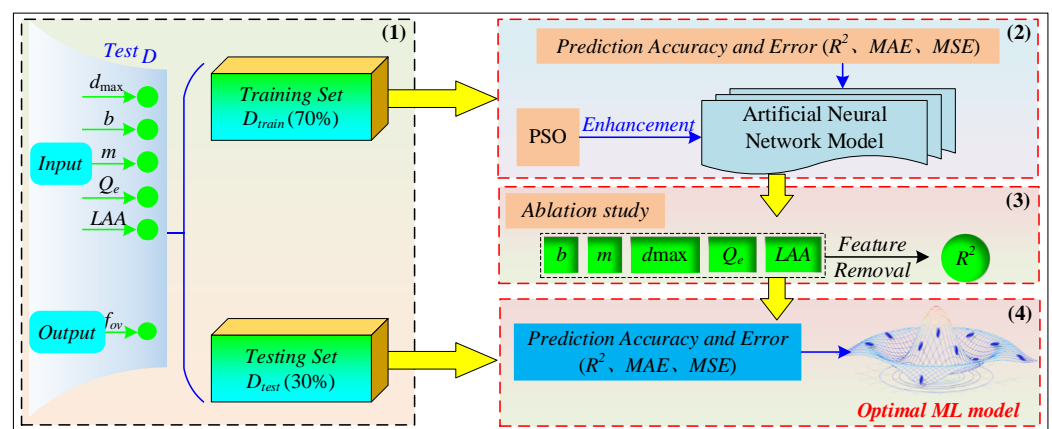


Figure 14. Schematic of ANN-based f_{ov} prediction model.

Step 1: Partitioning the dataset.

The dataset D was divided into training and testing sets in a 7:3 ratio, where the training set was used to develop the ML prediction model, and the testing set was used to evaluate the performance of the ANN-PM.

Step 2: Developing the ANN-PM based on the training set.

The ANN model was employed to predict f_{ov} , while the *particle swarm optimization* (PSO) algorithm [39,40] was introduced to optimize the hyperparameters of the ANN-PM. This method has been confirmed as an effective approach for hyperparameter optimization [41]. After that, the training set was inputted into the ANN-PM, and it was trained based on the optimal hyperparameters. The goodness-of-fit R^2 [42], mean square error (MSE) [43], and mean absolute error (MAE) [44] were used to evaluate the generalization ability of the ANN-PM.

Step 3: Evaluating the impact of key features on the ANN-PM performance based on the ablation study.

A series of prediction experiments was designed by removing key features to explore their impact on the ANN-PM predictive performance [45]. Similarly, R^2 was employed to evaluate the predictive performance of ANN-PM under different experimental conditions.

Step 4: Evaluating the performance of the ANN-PM based on the testing set.

After the ANN-PM was developed, the testing set was used for f_{ov} prediction. To quantify the generalization ability of the ANN-PM, the same evaluation criteria (R^2 , MAE, and MSE) for prediction accuracy and error as in step 2 were applied to evaluate the predictive performance of the ANN-PM.

3.4. Sensitivity Analysis of ANN-PM

As shown in Figure 15, based on the Monte Carlo method, the random fluctuations in ANN-PM input data could propagate through the output solution [46,47]. Then, the quantitative analysis of the probability distribution of the output solution could characterize the robustness of the ANN-PM.

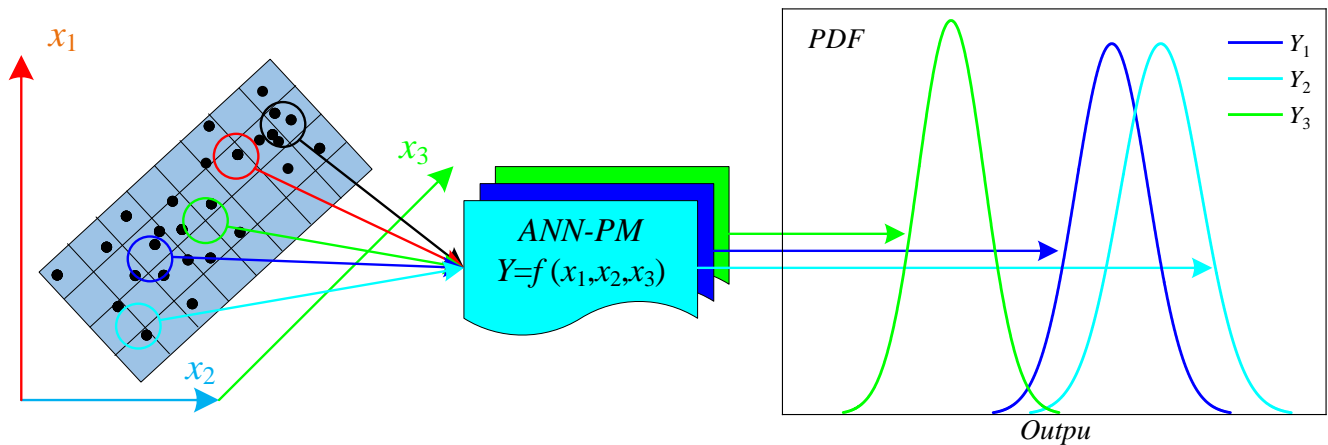


Figure 15. Schematic of the Monte Carlo method.

To comprehensively evaluate the ANN-PM performance, the Monte Carlo method was employed to simulate the probability distributions of R^2 and MSE . This analysis aimed to evaluate the robustness of the predictive models. The specific steps were outlined as follows:

Step 1: Randomization of data and result computation.

Randomizing the training set involves randomly combining 70% of the data for training and making predictions on the testing set. A set of $M-R^2$ and $M-MSE$ was calculated based on the predicted results, as shown in Equations (7) and (8).

$$M - R^2 = f_{R^2}(x_1, x_2, \dots, x_n) \quad (7)$$

$$M - MSE = f_{MSE}(x_1, x_2, \dots, x_n) \quad (8)$$

where $M-R^2$ and $M-MSE$ are the R^2 and MSE obtained through the Monte Carlo method. $f_{R^2}()$ and $f_{MSE}()$ denote the non-linear functions between the random input training set, the R^2 , and MSE .

Step 2: Repetitive simulation.

The number of Monte Carlo simulations was set to 300. Next, the computational process outlined in step 1 was repeated, resulting in N sets of $M-R^2$ and $M-MSE$, which were used to create probability distribution plots for structural analysis.

4. Results and Analysis

4.1. Establishment of ANN-PM Based on the Training Set

Figure 16 shows the variation of fitness for the ANN-PM during the iterative. It was clear that, with the iterative optimization of the PSO algorithm, the fitness of the ANN-PM significantly decreases and tends to stabilize after fewer iterations. This indicated that the PSO algorithm has a significant advantage in improving the prediction accuracy of ANN-PM. The optimum hyperparameters of the used ANN-PM in this paper were shown in Table 3. Furthermore, the obtained optimal hyperparameters were inputted into the ANN-PM for the prediction of f_{ov} .

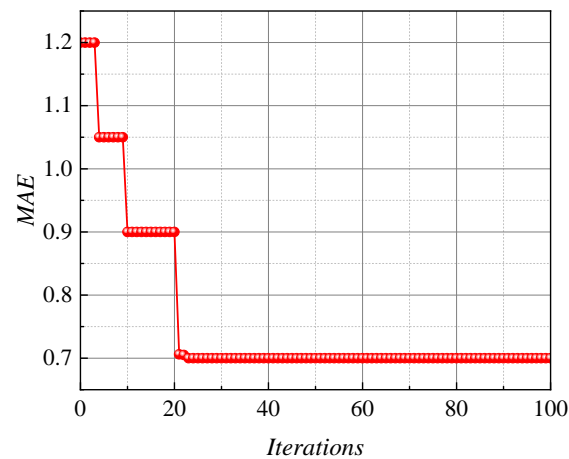


Figure 16. MAE values versus some iterations using hybrid models.

Table 3. Optimum hyperparameters of ANN models.

Hyperparameters	α	Neurons1	Neurons2	Epoch	Batch Size
ANN	0.001	100	100	200	16

As shown in Figure 17a, the scatter plot showed the fitting results of the ANN-PM on the training set, indicating the relationship between the predicted and actual values of f_{ov} . The horizontal axis represented the actual values of f_{ov} , while the vertical axis represented the predicted values. The more concentrated the data points were on the 45° median axis, the better fitting capability of the ANN-MLPM. The data points of the ANN-PM generally fluctuated around the 45° median axis, with the majority of points concentrated within the 10% error range, and only a small number of points fell outside this range, indicating that the ANN-PM demonstrated good fitting capability.

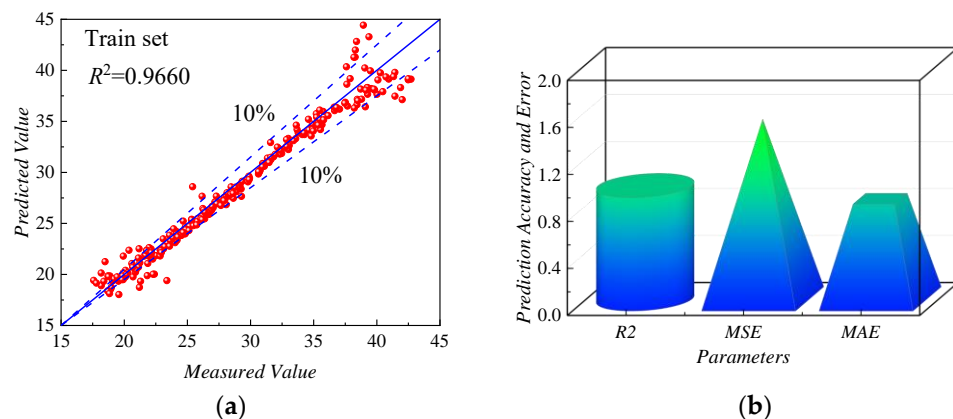


Figure 17. Predictive performance of ANN-PM in the training dataset: (a) R^2 , (b) R^2 , MSE, and MAE.

As shown in Figure 17b, the predictive performance of the ANN-PM on the training set was evaluated from the perspective of prediction accuracy and error. On the training set, the error indicators MAE (0.85391 Hz) and MSE (1.53176 Hz) of the ANN-PM were both small. Additionally, the R^2 of the ANN-PM was higher than 0.96, indicating a high level of fitting accuracy. However, the predictive results on the training set only indicated the predictive ability of the ANN-PM during the development of the model. Hence, the predictive performance of the ANN-PM should have been evaluated using the testing set.

4.2. Evaluating the Impact of Key Features on the ANN-PM Performance

As shown in Figure 18, when five features were used as input features, the ANN-PM achieved the highest R^2 , indicating the highest prediction accuracy. Subsequently, after removing the LAA, the R^2 of the ANN-PM was 0.9235, which only decreased by approximately 0.035. This indicated that the importance of the LAA for prediction results was relatively low. Conversely, when the d_{\max} was removed, the R^2 of the ANN-PM dropped to 0.8956, falling below 0.9. Similarly, when the d_{\max} was removed, MAE and MSE all reached their maximum values. This indicated that the d_{\max} held significant importance for prediction results. A comparative analysis revealed the importance rankings of the individual metrics as follows: $d_{\max} > b > m > Q_e > LAA$.

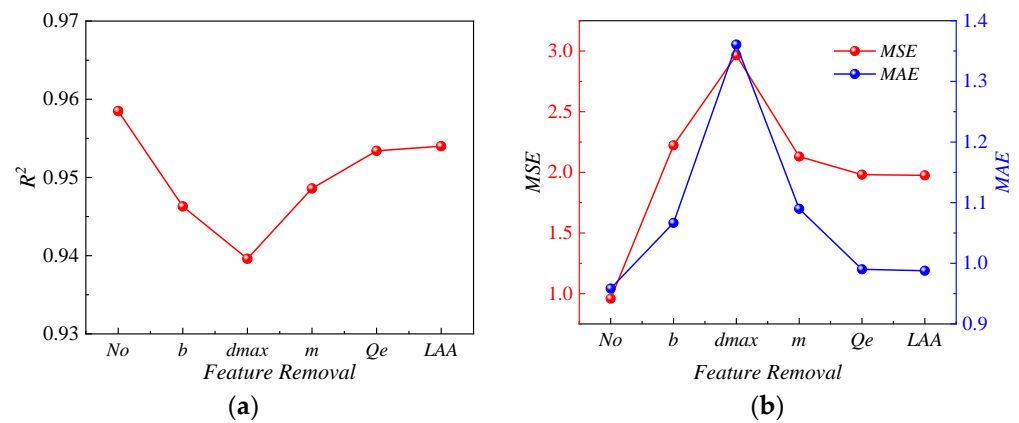


Figure 18. The results of the ablation study: (a) R^2 , (b) MSE and MAE.

4.3. Evaluation of ANN-PM Based on the Testing Set

As shown in Figure 19a, the scatter plot showed the fitting results of the ANN-PM on the testing set, indicating the relationship between the predicted and actual values of f_{ov} . The data points of the ANN-PM generally fluctuated around the 45° median axis, with the majority of points concentrated within the 10% error range, and only a small number of points fell outside this range, indicating that the ANN-PM demonstrated good fitting capability. As shown in Figure 19b, the predictive performance of the ANN-PM on the testing set was evaluated from the perspective of prediction accuracy and error. On the testing set, the error indicators MAE (1.05942 Hz) and MSE (1.93091 Hz) of the ANN-PM were both small. Additionally, the R^2 of the MLPM was higher than 0.95, indicating a high level of fitting accuracy.

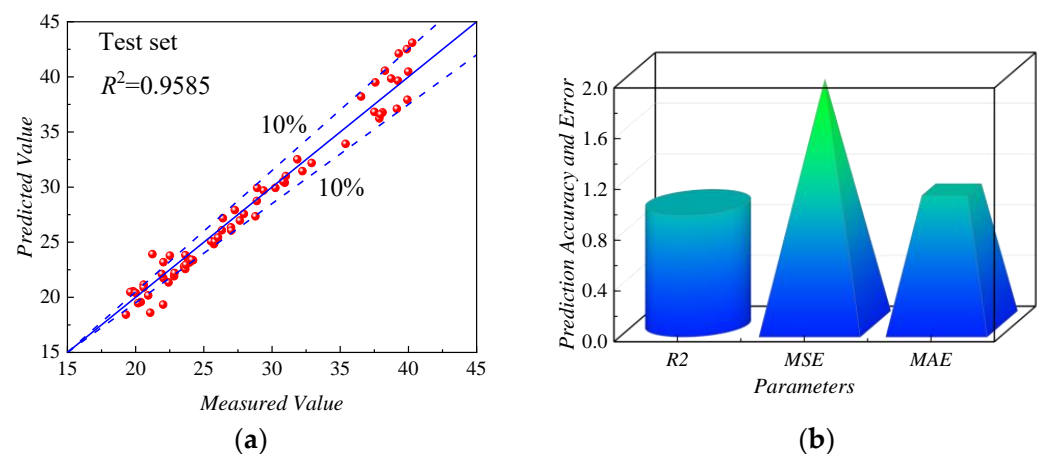


Figure 19. Predictive performance of ANN-PM in the test dataset: (a) R^2 , (b) R^2 , MSE, and MAE.

Based on the above, the *ANN-PM* showed good predictive performance in terms of prediction accuracy and error evaluation on both the training and testing sets. Hence, the *ANN-PM* could be employed to predict the f_{ov} for the vibratory compaction of *HRGG* fillers.

4.4. Sensitivity Analysis of *ANN-PM*

As shown in Figure 20, the probability distributions of the R^2 and *MSE* were obtained by the Monte Carlo analysis. The distribution of R^2 for the *ANN-PM* closely approached 1, with its mean value exceeding 0.9. This indicated that the *ANN-PM* maintained a high level of predictive accuracy. Simultaneously, the *MSE* distribution for the *ANN-PM* approached zero. Combining the robustness analysis results of R^2 and *MSE*, it was clear that the *ANN-PM* exhibited excellent robust performance.

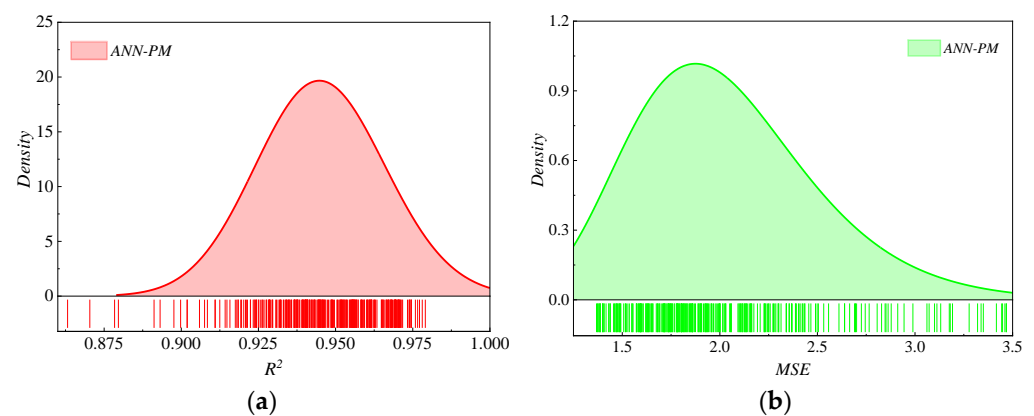


Figure 20. Results of the Monte Carlo method: (a) R^2 , (b) *MSE*.

5. Discussion

Based on the results of this paper and the references [11,21,48], it is indicated that the *ANN* model exhibits excellent predictive performance for the vibration compaction parameters (f_{ov}) of *HRGG* fillers. This highlights the significant advantage of the *ANN* model in f_{ov} prediction, providing more accurate guidance for practical engineering applications. Hence, in forthcoming f_{ov} prediction applications, especially in the field of intelligent compaction, the *ANN* model is poised to become a potent tool. As intelligent technologies continue to evolve, this model has the potential to deliver accurate f_{ov} predictions for practical engineering, further propelling the advancement of intelligent compaction control. Nevertheless, there are still some issues that require further optimization regarding the *ANN* model. Despite demonstrating excellent predictive capabilities, the black-box nature of the *ANN* can hinder its real-world applications due to a lack of transparency in decision making. Hence, an in-depth exploration of data augmentation and model interpretability techniques can enhance the robustness of predictive results. Given these limitations, future research could employ SHapley Additive exPlanations (*SHAP*) analysis to reveal the relative importance of different input features. Moreover, the integration of advanced techniques such as ensemble learning or hybrid models may further improve prediction accuracy and reduce potential uncertainties.

6. Conclusions

To address the uncertainty of optimal vibratory frequency f_{ov} of high-speed railway graded gravel (*HRGG*) and achieve high-precision prediction of the f_{ov} , the following research was conducted. Firstly, the correlation between the resonance frequency f_0 and f_{ov} of fillers with different compactness K was determined by vibratory compaction experiments and the hammering modal analysis method. Secondly, the relationship between the filler feature and f_{ov} was established, which revealed the key feature influencing the f_{ov} . Finally, the artificial neural network prediction model (*ANN-PM*) for predicting f_{ov} was established based on the key characteristics. The ablation study, prediction errors, and accuracy were

used to evaluate the predictive performance of ANN-PM. Furthermore, the ANN-PM robust performance was evaluated based on the sensitivity analysis. The main conclusions obtained are as follows:

1. In the vibratory compaction experiments, maximum dry density ρ_{dmax} , stiffness K_{rd} , and bearing capacity coefficient K_{20} of different gradation HRGG fillers all obtained optimal states when the vibratory frequency was set as f_0 , which indicated that f_0 was the f_{ov} .
2. Based on the gray relational analysis algorithm, the key features influencing the f_{ov} were determined to be the maximum particle diameter d_{max} , gradation parameters b and m , flat and elongated particles in coarse aggregate Q_e , and the Los Angeles abrasion of coarse aggregate LAA .
3. The key feature influencing the f_{ov} was used to establish the ANN-PM. Then, based on the ablation study, it was indicated that the impact hierarchy of the five key features on the ANN-PM predictive performance was $d_{max} > b > m > Q_e > LAA$.
4. On the training and testing sets, the goodness-of-fit R^2 of ANN-PM all exceeded 0.95, and the prediction errors were small, which indicated the strong prediction capability of ANN-PM for f_{ov} .
5. Based on the sensitivity analysis, the distribution of R^2 for the ANN-PM closely approached 1, with its mean value exceeding 0.9. In addition, the MSE distribution for the ANN-PM approached zero. It was clear that the ANN-PM exhibited excellent robust performance.

Author Contributions: Conceptualization, X.X. and T.L.; methodology, X.X.; software, Z.H.; validation, X.L. and X.X.; formal analysis, X.X.; investigation, Z.H.; resources, T.L.; data curation, X.L.; writing—original draft preparation, X.X.; writing—review and editing, F.L. and J.L.; visualization, F.L. and J.L.; supervision, X.X.; project administration, Z.H.; funding acquisition, T.L. All authors have read and agreed to the published version of the manuscript.

Funding: This work was funded by the National Key R&D Program “Transportation Infrastructure” project, grant number 2022YFB2603400.

Institutional Review Board Statement: Not applicable.

Informed Consent Statement: Not applicable.

Data Availability Statement: Data are contained within the article.

Conflicts of Interest: Author Taifeng Li was employed by the China Academy of Railway Sciences Co., Ltd. The remaining authors declare that the research was conducted in the absence of any commercial or financial relationships that could be construed as a potential conflict of interest.

References

1. Qu, L.; Yang, C.; Ding, X.; Kouroussis, G.; Yuan, C. Vertical vibration of piles with a square cross-section. *Int. J. Numer. Anal. Met.* **2021**, *45*, 2629–2653. [[CrossRef](#)]
2. Wan, Z.; Bian, X.; Li, S.; Chen, Y.; Cui, Y. Remediation of mud pumping in ballastless high-speed railway using polyurethane chemical injection. *Constr. Build. Mater.* **2020**, *259*, 120401. [[CrossRef](#)]
3. Lian, J.; Ding, X.; Cai, D.; Yue, M. Intelligent adaptive control method for key parameters of vibration rolling during high-speed railway subgrade compaction. *Transp. Geotech.* **2023**, *41*, 101000. [[CrossRef](#)]
4. Ye, Y.S.; Cai, D.G.; Zhang, Q.L.; Wei, S.W.; Yan, H.Y.; Geng, L. Review on vibration compaction theory and intelligent compaction technology of high-speed railway subgrade. *China Railw. Sci.* **2021**, *42*, 1–12. (In Chinese)
5. Bian, X.; Li, W.; Qian, Y.; Tutumluer, E. Analysing the effect of principal stress rotation on railway track settlement by discrete element method. *Géotechnique* **2020**, *70*, 803–821. [[CrossRef](#)]
6. Sadek, Y.; Rikioui, T.; Abdoun, T.; Dadi, A. Influence of Compaction Energy on Cement Stabilized Soil for Road Construction. *Civil. Eng.* **2022**, *8*, 580–594. [[CrossRef](#)]
7. Xie, K.; Su, Q.; Chen, X.B.; Liu, B.; Wang, W.B.; Wang, X.; Deng, Z.X. Element model test on polyurethane crushed stone waterproof bonding layer of ballastless track. *Rock Soil Mech.* **2023**, *44*, 1–11. (In Chinese)
8. Yang, C.W.; Zhang, L.; Su, K. Research on dynamic response of railway subgrade packing vibration compaction based on VMD-Hilbert transform. *Chin. J. Rock Mech. Eng.* **2022**, *41* (Suppl. S1), 2991–3001. (In Chinese)

9. Wang, M.; Yu, Q.D.; Xiao, Y.J.; Li, W.Q.; Hua, W.J.; Wang, X.M.; Chen, X.B. Experimental investigation of macro-and meso-scale compaction characteristics of unbound permeable base materials. *Chin. J. Rock Mech. Eng.* **2022**, *41*, 1701–1716. (In Chinese)
10. Ji, X.; Lu, H.; Dai, C.; Ye, Y.; Cui, Z.; Xiong, Y. Characterization of Properties of Soil-Rock mixture prepared by the laboratory vibration compaction method. *Sustainability* **2021**, *13*, 11239. [CrossRef]
11. Xie, K.; Li, T.-F.; Chen, X.-B.; Deng, Z.-X. A novel method for determining the particle breakage contribution of high-speed railway graded aggregate and its application in vibratory compaction. *Case. Stud. Constr. Mat.* **2023**, *19*, e02281. [CrossRef]
12. Ye, Y.S.; Chen, X.B.; Hui, X.H.; Cai, D.G.; Yao, J.K.; Jin, L.X. Laboratory investigation on parameter optimization of vibrating compaction for high-speed railway's group B. *J. Railw. Sci. Eng.* **2021**, *18*, 2497–2505. (In Chinese)
13. Zhang, Q.; Liu, T.; Zhang, Z.; Huangfu, Z.; Li, Q.; An, Z. Compaction quality assessment of rockfill materials using roller-integrated acoustic wave detection technique. *Automa. Constr.* **2019**, *97*, 110–121. [CrossRef]
14. Li, J.; Zhou, Z.L.; Li, Y. Test analysis of relationship between natural frequency and compaction degree for roadbed soil. *Trans. Chin. Soc. Agric. Eng.* **2012**, *28*, 71–76. (In Chinese)
15. Xie, K.; Chen, X.B.; Yao, J.K.; Cai, D.G. Study on standardization method and application of vibration compaction test parameters of high-speed railway subgrade filler. *Chin. J. Rock Mech. Eng.* **2023**, *42*, 1799–1810. (In Chinese)
16. Hu, W.; Polaczyk, P.; Jia, X.; Gong, H.; Huang, B. Visualization and quantification of lab vibratory compacting process for aggregate base materials using accelerometer. *Transp. Geotech.* **2020**, *25*, 100393. [CrossRef]
17. Liu, J.; Yang, X. Learning to See the Vibration: A Neural Network for Vibration Frequency Prediction. *Sensors* **2018**, *18*, 2530. [CrossRef] [PubMed]
18. Quan, T.V.; Quoc, D.V.; Si, H.L. Evaluating compressive strength of concrete made with recycled concrete aggregates using machine learning approach. *Constr. Build. Mater.* **2022**, *323*, 126578. [CrossRef]
19. Isik, F.; Ozden, G. Estimating compaction parameters of fine- and coarse-grained soils by means of artificial neural networks. *Environ. Earth. Sci.* **2013**, *69*, 2287–2297. [CrossRef]
20. Zaman, M.; Solanki, P.; Ebrahimi, A.; White, L. Neural network modeling of resilient modulus using routine subgrade soil properties. *Int. J. Geomech.* **2010**, *10*, 1–12. [CrossRef]
21. Xie, K.; Chen, X.-B.; Li, T.-F.; Deng, Z.-X.; Yao, J.-K.; Tang, L.-B. A framework for determining the optimal moisture content of high-speed railway-graded aggregate materials based on the lab vibration compaction method. *Constr. Build. Mater.* **2023**, *392*, 131764. [CrossRef]
22. Jayan, J.; Sankar, N. Prediction of compaction parameters of soils using artificial neural network. *Asian J. Eng. Technol.* **2015**, *3*, 2321–2462.
23. Kolakoti, A.; Prasadarao, B.; Satyanarayana, K.; Setiyo, M.; Köten, H.; Raghu, M. Elemental, Thermal and physicochemical investigation of novel biodiesel from wodyetia bifurcata and its properties optimization using artificial neural network (ANN). *Automot. Exp.* **2022**, *5*, 2615–6636. [CrossRef]
24. TB10001-2016; Code for Design of Railway Earth Structure. Ministry of the Railway: Beijing, China, 2016. (In Chinese)
25. Xie, K.; Chen, X.B.; Yao, J.K.; Li, T.F.; Wang, Y.S.; Deng, Z.X.; Lv, X.L. Study on the Vibration Compaction Mechanism with High-Speed Railway Fillers Based on the Dynamic Evolution of Coarse Particles. *Chin. J. Geotech. Eng.* 1–10. Available online: <http://kns.cnki.net/kcms/detail/32.1124.tu.20230818.1510.002.html> (accessed on 21 August 2023). (In Chinese)
26. Chen, X.L.; Wang, Y.H.; Wang, C.H. Modal analysis and experiment research on natural frequencies of transition section subgrade of high-speed railway. *J. Cent. South Univ. (Sci. Technol.)* **2012**, *43*, 322–327. (In Chinese)
27. TB/T 2140-2008; Railway Ballast. China Railway Publishing House: Beijing, China, 2008.
28. TB 10102-2023; Geotechnical Testing Procedures for Railway Engineering. China Railway Publishing House: Beijing, China, 2023.
29. Fan, Y.B.; Liu, C.; Wang, J.B. Prediction algorithm for springback of frame-rib parts in rubber forming process by incorporating Sobol within improved grey relation analysis. *J. Mater. Res. Technol.* **2021**, *13*, 1955–1966. [CrossRef]
30. Wu, E.-L.; Zhu, J.-G.; Chen, G.; Wang, L. Experimental study of effect of gradation on compaction properties of rockfill materials. *Bull. Eng. Geol. Environ.* **2020**, *79*, 2863–2869. [CrossRef]
31. Armaghani, D.J.; Asteris, P.G. A comparative study of ANN and ANFIS models for the prediction of cement-based mortar materials compressive strength. *Neural. Comput. Appl.* **2021**, *33*, 4501–4532. Available online: <https://link.springer.com/article/10.1007/s00521-020-05244-4> (accessed on 24 July 2020).
32. Jalal, M.; Grasley, Z.; Gurganus, C.; Bullard, J.W. A new nonlinear formulation-based prediction approach using artificial neural network (ANN) model for rubberized cement composite. *Eng. Comput.* **2022**, *38*, 283–300. Available online: <https://link.springer.com/article/10.1007/s00366-020-01054-3> (accessed on 15 May 2020).
33. Escribano, A.; Wang, D. Mixed random forest, cointegration, and forecasting gasoline prices. *Int. J. Forecast.* **2021**, *37*, 1442–1462. [CrossRef]
34. Han, H.; Shi, B.; Zhang, L. Prediction of landslide sharp increase displacement by SVM with considering hysteresis of groundwater change. *Eng. Geol.* **2021**, *280*, 105876. [CrossRef]
35. Latif, S.D. Developing a boosted decision tree regression prediction model as a sustainable tool for compressive strength of environmentally friendly concrete. *Environ. Sci. Pollut. Res.* **2021**, *28*, 65935–65944. Available online: <https://link.springer.com/article/10.1007/s11356-021-15662-z> (accessed on 22 July 2021).
36. Ren, X.; Yang, B.; Luo, N.; Li, J.; Li, Y.; Xue, T.; Yang, A. The Prediction of Sinter Drums Strength Using Hybrid Machine Learning Algorithms. *Comput. Intell. Neurosci.* **2022**, *2022*, 4790736. [CrossRef] [PubMed]

37. Fareeha, A.; Chen, W.X. Investigation of steam ejector parameters under three optimization algorithm using ANN. *Appl. Therm. Eng.* **2023**, *225*, 120205. [[CrossRef](#)]
38. Hu, R.; Monebhurrun, V.; Himeno, R.; Yokota, H.; Costen, F. A General Framework for Building Surrogate Models for Uncertainty Quantification in Computational Electromagnetics. *IEEE Trans. Antennas Propag.* **2022**, *70*, 1402–1414. [[CrossRef](#)]
39. Song, M.; Ge, Y.H.; Liu, J.S. Improved Dynamic Dual Adaptive PSO Algorithm Based on Theory of Co-evolution. *Comput. Eng. Appl.* **2020**, *56*, 54–62. (In Chinese)
40. Deng, Z.-X.; Xie, K.; Su, Q.; Xu, L.-R.; Hao, Z.-R.; Xiao, X.-P. Three-level evaluation method of cumulative slope deformation hybrid machine learning models and interpretability analysis. *Constr. Build. Mater.* **2023**, *408*, 133821. [[CrossRef](#)]
41. Ghannadi, P.; Kourehli, S.S.; Mirjalili, S. The Application of PSO in Structural Damage Detection: An Analysis of the Previously Released Publications (2005–2020). *Frat. Ed Integrità Strutt.* **2022**, *16*, 460–489. [[CrossRef](#)]
42. Zeng, Z.; Zhu, Z.; Yao, W.; Wang, Z.; Wang, C.; Wei, Y.; Wei, Z.; Guan, X. Accurate prediction of concrete compressive strength based on explainable features using deep learning. *Constr. Build. Mater.* **2022**, *329*, 127082. [[CrossRef](#)]
43. Cheng, Y.; Zhou, W.H.; Xu, T. Tunneling-induced settlement prediction using the hybrid feature selection method for feature optimization. *Transp. Geotech.* **2022**, *36*, 100808. [[CrossRef](#)]
44. Zhang, P.; Wu, H.-N.; Chen, R.-P.; Chan, T.H. Hybrid meta-heuristic and machine learning algorithms for tunneling-induced settlement prediction: A comparative study. *Tunn. Undergr. Space. Technol.* **2020**, *99*, 103383. [[CrossRef](#)]
45. Younas, J.; Malik, M.I.; Ahmed, S.; Shafait, F.; Lukowicz, P. Sense the pen: Classification of online handwritten sequences (text, mathematical expression, plot/graph). *Expert. Syst. Appl.* **2021**, *15*, 114588. [[CrossRef](#)]
46. Zhang, Y.G.; Zhao, Y.P.; Shen, X.Y.; Zhang, J. A comprehensive wind speed prediction system based on Monte Carlo and artificial intelligence algorithms. *Appl. Energ.* **2022**, *305*, 117815. [[CrossRef](#)]
47. Zhao, X.; Ge, C.; Ji, F.; Liu, Y. Monte Carlo Method and Quantile Regression for Uncertainty Analysis of Wind Power Forecasting Based on Chaos-LS-SVM. *Int. J. Control Autom.* **2021**, *19*, 3731–3740. [[CrossRef](#)]
48. Zheng, W.H. A novel method for dry density forecasting of high-speed railway graded aggregate fillers based on the PSO-ANN model. *Results Eng.* **2023**, *19*, 101361. [[CrossRef](#)]

Disclaimer/Publisher’s Note: The statements, opinions and data contained in all publications are solely those of the individual author(s) and contributor(s) and not of MDPI and/or the editor(s). MDPI and/or the editor(s) disclaim responsibility for any injury to people or property resulting from any ideas, methods, instructions or products referred to in the content.